# MXene/Nitrogen-Doped Carbon Nanosheet Scaffold Electrode toward High-Performance Solid-State Zinc Ion Supercapacitor

*Anli Chen, Huige Wei,\* Zhuojian Peng, Yuanzhe Wang, Stephen Akinlabi, Zhanhu Guo, Faming Gao,\* Sidi Duan, Ximin He,\* Chunjiang Jia, and Ben Bin Xu\**

While MXene is widely used as an electrode material for supercapacitor, the intrinsic limitation of stacking caused by the interlayer *van der Waals* forces has yet to be overcome. In this work, a strategy is proposed to fabricate a composite scaffold electrode (MCN) by intercalating MXene with highly nitrogen-doped carbon nanosheets (CN). The 2D structured CN, thermally converted and pickling from Zn-hexamine (Zn-HMT), serves as a spacer that effectively prevents the stacking of MXene and contributes to a hierarchically scaffolded structure, which is conducive to ion movement; meanwhile, the high nitrogen-doping of CN tunes the electronic structure of MCN to facilitate charge transfer and providing additional pseudocapacitance. As a result, the MCN50 composite electrode achieves a high specific capacitance of 418.4 F g$^{-1}$ at 1 A g$^{-1}$. The assembled symmetric supercapacitor delivers a corresponding power density of 1658.9 W kg$^{-1}$ and an energy density of 30.8 Wh kg$^{-1}$. The all-solid-state zinc ion supercapacitor demonstrates a superior energy density of 68.4 Wh kg$^{-1}$ and a power density of 403.5 W kg$^{-1}$ and shows a high capacitance retention of 93% after 8000 charge-discharge cycles. This study sheds a new light on the design and development of novel MXene-based composite electrodes for high performance all-solid-state zinc ion supercapacitor.

## 1. Introduction

Driven by the Net Zero agenda, renewable energies such as wind, wave, and solar energy have sparked significant advancements to replace fossil fuel. These renewable energies also present intermittent characteristics and cannot provide stable energy output, which usually requires energy storage.[1] Supercapacitor has attracted increasing attention for its high power density and exceptional cycling stability,[2] enabling great energy storage application potentials in wearable and portable electronics, high-performance electric vehicles, etc.[3] The electrode materials determines the performance of supercapacitors, and are generally classified into carbon materials,[2b] conducting polymers,[4] and transitional metal oxides.[5] Unfortunately, challenges such as low energy density and poor rate performance remain to be tackled.

The 2D layered materials, like graphene,[6] transition metal dihalides,[7] and layered double hydroxides (LDHs),[8] have been widely employed to develop supercapacitor electrode due to their distinctive physicochemical properties. MXene, a novel 2D material composed of transition metal carbides and nitrides with metallic conductivity, has emerged as a leading candidate in the energy storage field such as supercapacitor and ion battery.[9] The generic formula for MXene can be represented as $M_{n+1}X_nT_x$ (where n = 1, 2, or 3), with M representing an early transition metal, X indicating either carbon (C) or nitrogen (N), and $T_x$ denoting functional groups such as –O, –F, or –OH.[10] Like other 2D materials, MXene is prone to stacking due to interlayer *van der Waals* forces, which hinders ion penetration

A. Chen, H. Wei, Z. Peng, Y. Wang, F. Gao
Tianjin Key Laboratory of Brine Chemical Engineering and Resource Eco-utilization, College of Chemical Engineering and Materials Science
Tianjin University of Science and Technology
Tianjin 300457, China
E-mail: huigewei@tust.edu.cn; fmgao@tust.edu.cn

S. Akinlabi, Z. Guo, B. B. Xu
Department of Mechanical and Construction Engineering
Northumbria University
Newcastle Upon Tyne NE1 8ST, UK
E-mail: ben.xu@northumbria.ac.uk
S. Duan, X. He
Department of Materials Science and Engineering
University of California Los Angeles (UCLA) Los Angeles
CA 90095, USA
E-mail: ximinhe@ucla.edu
C. Jia
Offshore Renewable Energy Catapult
Offshore House, Albert Street, Blyth NE24 1LZ, UK

**ADVANCED
SCIENCE NEWS**

www.advancedsciencenews.com

**NANO · MICRO
small**

www.small-journal.com

and reduces surface active sites accessible to electrolytes.[11] Continuous efforts have been devoted to increase the lamellar spacing of MXene by introducing intercalating agents or spacers such as graphene,[12] carbon nanotubes,[13] and conductive polymers.[14] Wen et al.[9a] developed flexible MXene/graphene composite electrodes with 75% capacitance retention after 3000 charge-discharge cycles. Ning and co-workers[15] reported a 3D structure composed of MXene, carbon nano coils, and poly(3,4-ethylene-dioxythiophene): poly(styrene sulfonate) (PEDOT:PSS), delivering an areal capacitance of 232 mF cm$^{-2}$ at 10 mV s$^{-1}$. Although the accessibility of ions was indeed improved by increasing the interlayer spacing; however, the electron conductivity was impaired arising from the highly porous structure. Therefore, an effective strategy is highly desired to resolve the stacking of MXene layers and promote the charge transfer kinetics for higher electrochemical performance.

Herein, we proposed a facile route to fabricate structural composite electrode (MCN) consisting of MXene intercalated with highly nitrogen-doped carbon nanosheets (CN) to form scaffold structure with 2D Zn-hexamine (Zn-HMT) coordination framework nanosheets as a self-sacrificial template. As an intercalator and carbon source of MXene, Zn-HMT has the following advantages. First, Zn-HMT coordination framework nanosheets were constructed using low cost $Zn(NO_3)_2$ as the metal centers and hexamethylenetetramine (HMT) as the ligands by simple droplet mixing and stirring. The positively charged Zn-HMT nanosheets readily combine with MXene by a facile and rapid electrostatic self-assembly process. The whole process is conducive to large-scale manufacturing. More importantly, Zn-HMT nanosheets are rich in nitrogen elements, and therefore, the resulting highly nitrogen-doped 2D CN thermally converted and pickling from Zn-HMT not only changes the electronic structure of the MXene, facilitating the ion transfer, but also creates defects and electronegative sites, introducing additional pseudocapacitance for the MCN electrode. Lastly, unlike other 2D materials, this nitrogenous CN derived from Zn-HMT scaffolds serve as spacers that effectively increases the layer spacing of MXene, and have a large number of openings, contributes to a hierarchically scaffolded structure, which is conducive to electrolyte exposure.[16] As such, the MCN composite electrode achieves a superior electrochemical performance. The all-solid-state zinc ion supercapacitor with MCN50 as electrode exhibits high capacitance, superior energy density and power density, and robust capacitance retention.

## 2. Results and Discussion

### 2.1. Preparation and Characterization of MCN Composite Scaffold Electrodes

Figure 1 shows the schematic preparation of MCNs and their morphology. MCN composite electrodes were prepared by the electrostatic self-assembly of Zn-HMT and MXene (Figure 1a), followed by the annealing and pickling treatments. 2D Zn-HMT coordination framework nanosheets were constructed using $Zn(NO_3)_2$ as the metal centers and HMT as the ligands.[17] The stratified MXene ($Ti_3C_2T_x$) was prepared by taking away the Al layer from the precursor MAX ($Ti_3AlC_2$) using HCl and LiF.[18] The diffraction peaks at 7°, 15°, and 20° of XRD pattern prove the formation of the coordination framework of Zn-HMT (Figure S1). In the FTIR spectrum (Figure S2), two prominent bands locating at 1000 and 1225 cm$^{-1}$ can be attributed to the stretching vibration of C-N principle of HMT. The split of these absorption bands into doublets further proves the coordination frameworks of Zn-HMT. Zn-HMT nanosheets are positively charged (+25.4 mV) whereas MXene nanosheets are negatively charged (−34.3 mV) as suggested by Zeta potential measurements (Figure S3). The electrostatic self-assembly process took place immediately by mixing MXene and Zn-HMT solutions. The precipitates were heated at 500°C in the argon atmosphere to acquire Zn-MCN. TGA curves in Figure S4 reveal that the weight losses of MXene, Zn-HMT, and MXene/Zn-HMT50 are 2.72%, 62.97%, and 13.17%, respectively, proving the conversion of Zn-HMT precursors into carbon nanosheets during the annealing process. The final MCN electrodes were obtained by pickling to remove Zn, thereby increasing the porosity in the composite.

The electrodes were characterized by SEM and TEM to observe the morphology and microstructure (Figure 1b-j). The smooth surface (Figure 1b, mono-dispersed MXene from aqueous solution) and the seriously stacked layer structure (Figure 1c, MXene obtained by vacuum filtration) is clearly observed in the SEM of MXene, as opposed to the dense structure of MAX (Figure S5). In addition, SAED (the inset of Figure S6) reveals the hexagonal structure of basal planes with a high degree of crystallinity of MXene nanosheets.[19] The Zn-HMT nanosheets exhibit a distinct 2D laminar structure (Figure 1d), and the single-layer nanosheet structure is also observed by TEM image (Figure 1e). In general, the structure of most MOFs is destroyed by electron beam irradiation, but Zn-HMT nanosheets are able to maintain a stable structure without obvious defects.[20] The SAED pattern further indicates the presence of stable polycrystalline phases in Zn-HMT (the inset of Figure 1e). Compared with the tightly packed structure of MXene, MXene/Zn-HMT50 has an obvious porous network, reflecting the effective intercalation of Zn-HMT (Figure 1f). After the annealing, the Zn-HMT exhibits a layered and moderately porous network structure (Figure 1g), and FESEM-EDS mappings shows the uniform distribution of Ti, N, O, C, and Zn elements (Figure S7).

The TEM image of MCN50 (Figure 1h) reveals homogeneous distribution of the carbonized nanosheets, with a wide layer distance of 1.09 nm shown for MXene. The SAED image of MCN (the inset of Figure 1h) shows a bright diffraction ring in the center, which is attributed to the carbonized Zn-HMT.[21] High-resolution TEM (HRTEM) in Figure 1i reveals that the carbon nanosheets have a layer spacing of 0.357 nm, indicating obvious graphite layers. The FESEM-EDS mappings of Ti, N, O, and C elements in Figure 1j prove that MXene and nitrogen-doped carbon nanosheets are uniformly distributed. In addition, the energy-dispersive X-ray spectroscopy of EDS mapping and element contents of Zn-MCN50 and MCN50 in Figure S8 and Table S1, respectively, proving the effective removal of Zn impurities. The nitrogen adsorption-desorption isotherm curves of MCN50 and MXene are shown in Figure S9. The specific surface area of MCN50 is calculated to be 76.8 m$^2$ g$^{-1}$, substantially higher than that of MXene (1.7 m$^2$ g$^{-1}$) which falls into the range of 1.7–38 m$^2$ g$^{-1}$ reported by other groups.[22] The pore size distribution (Figure S10) indicates that MCN50 primarily consists of micropores measuring 1.02 nm and mesopores measuring 3.72 nm,
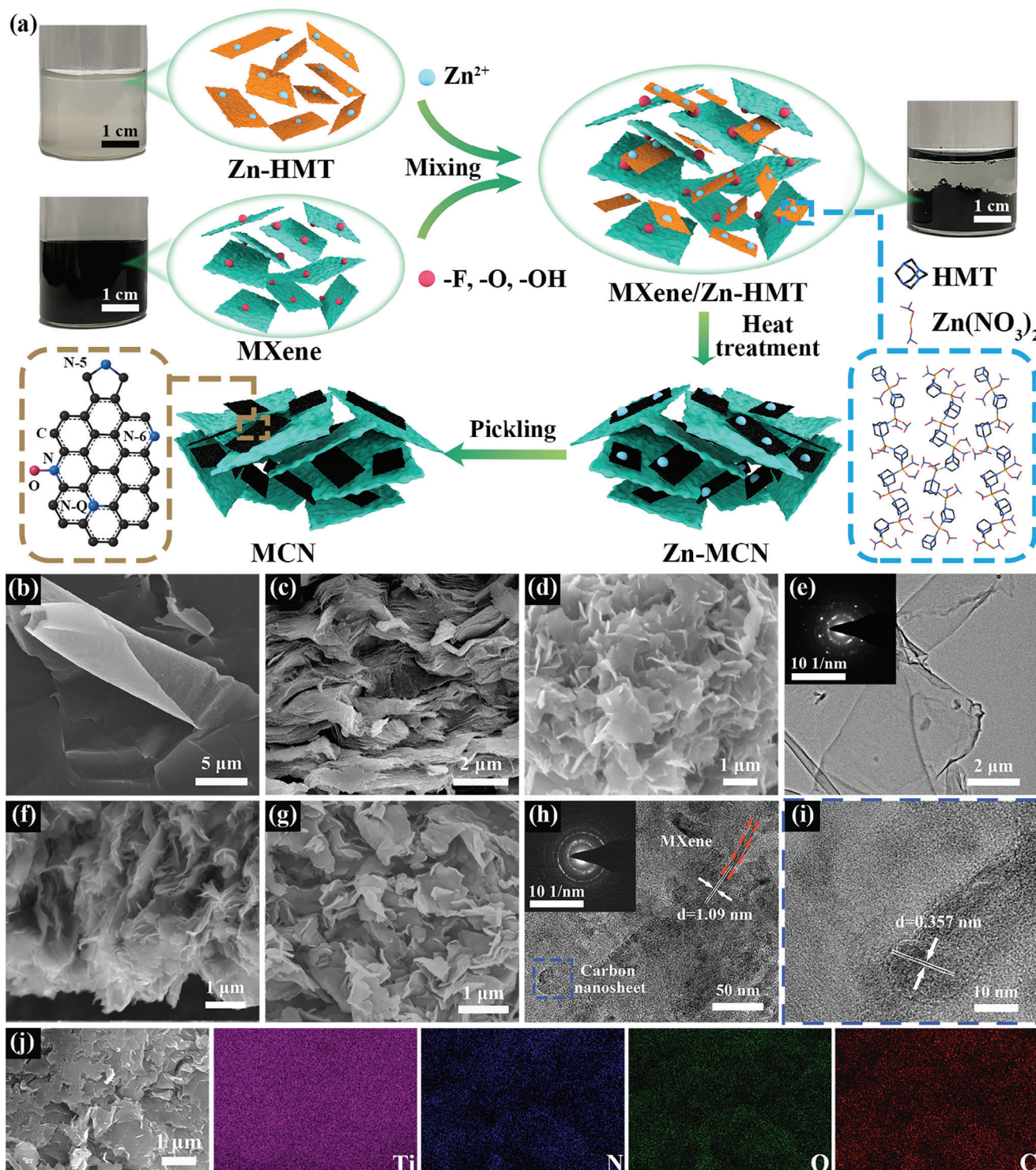
**Figure 1.** Schematic preparation of MCNs and the morphology. a) Schematic illustration of fabricating MCNs. SEM image of b) mono-dispersed MXene from aqueous solution and (c) MXene obtained by vacuum filtration. d) SEM and e) TEM images of Zn-HMT (the inset is the SAED). SEM images of f) MXene/Zn-HMT50 and g) MCN50. h) TEM images of MCN50 (the inset is the SAED) and i) high resolution lattice fringes. j) Elemental mapping of MCN50 showing Ti, N, O, C elements.
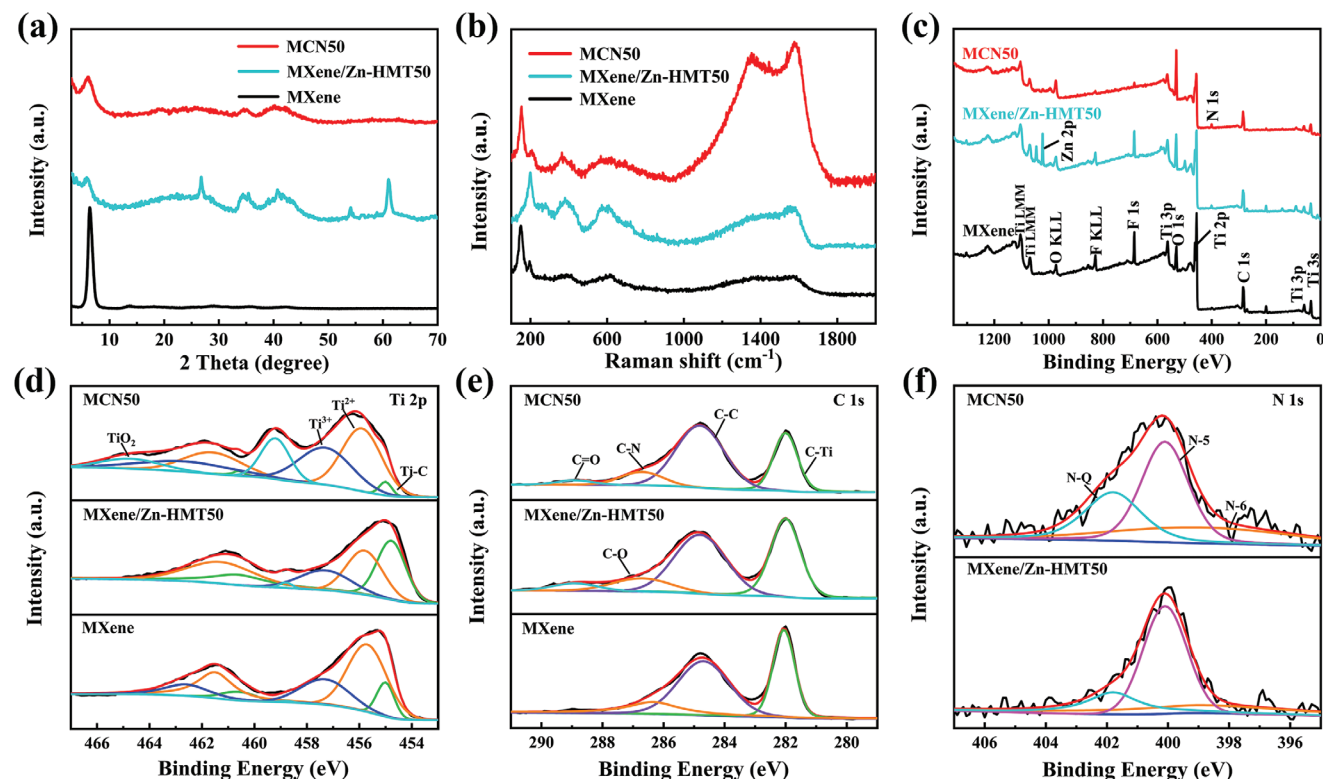
**Figure 2.** Crystalline and chemical structure of MCNs. a) XRD patterns, b) Raman spectra, and c) XPS survey spectra of MXene, MXene/Zn-HMT50, and MCN50. The high resolution spectrum of d) Ti 2p, e) C 1s, f) N 1s region.

while MXene is mainly composed of 2.10 nm and 4.36 nm mesopores. The distance between MXene layers is mainly responsible for the formation of mesopores during the preparation. For MCN50, the micropores are formed by the removal of Zn impurities, while mesopores are mainly constructed by the electrostatic self-assembly process. In this hierarchically porous structure of MCN50, the presence of micropores enhances the specific surface area and facilitates the exposure of additional active sites, while the mesopores are more conducive to rapid ion migration in the electrolyte under higher current density. Moreover, multiple micropores can be connected through the mesopores, effectively improving ion transfer efficiency, speeding up the transfer of ions from the surface to the body of the electrode, so as to maximize the ability of micropores to store energy.[23]

Crystalline and chemical structure of MCN50 were displayed in **Figure 2**. XRD patterns of MXene, MXene/Zn-HMT50, and MCN50 are displayed in Figure 2a. The (002) peak in XRD patterns of MXene indicates an ordered arrangement of MXene nanosheets due to self-accumulation.[24] The (002) diffraction peak shifts from 6.03° in MXene to 5.86° in MCN50, indicating an increase in d-spacing from 14.72 Å in MXene to 15.06 Å in MCN50 This shift is evidence of Zn-HMT intercalation in MXene. In addition, the intensity of (002) peak in MCN50 is significantly reduced, indicating decreased stacking of MXene by the intercalation.[25] Raman spectrum in Figure 2b observes no D or G peaks for MXene, indicating no free carbons.[26] The $I_D/I_G$ values MCN50 is 0.91, respectively, indicating amorphous carbon structure.

In the XPS survey spectra (Figure 2c), the MCN50 curve contains a sharp N1s peak (398.4 eV) compared to pure MXene, proving N-doping in MCN50.[27] As MXene/Zn-HMT50 is converted to MCN50, the Zn 2p peak (1022 eV) almost completely disappears, indicating that the Zn impurities have been removed by the acid washing. The Ti 2p peak can be fitted into five components centered at 455.0 eV (460.6 eV), 455.8 eV (461.3 eV), 457.3 eV (462.6 eV), and 458.8 eV (464.4 eV), corresponding to the Ti-C, Ti$^{2+}$, Ti$^{3+}$, and TiO$_2$ bonds, respectively (Figure 2d).[10b] The C 1s spectra in Figure 2e can be resolved into four peaks at 282,2, 284.8, 286.7, and 288.9 eV, corresponding to C-Ti, C-C, C-O, and C = O, respectively.[28] In addition, the introduction of N element forms the C-N bond, which leads to a significant increase in the peak intensity at 286.7 eV in MCN50. Compared to our previous work[10b] with 1.90 at.% of nitrogen for the nitrogen-doped carbon nanospheres intercalated MXene, the nitrogen content in MCN50 is much higher, with an atomic percentage of 3.64 at.% (Table S2). Moreover, although nitrogen-doped carbon nanospheres as intercalators in the previous study could construct a porous network structure that was conducive to ion transport, the porous structure also hindered electron conductivity. On the contrast, nitrogen-doped carbon nanosheets can not only promotes ion transport, but also enhances electron transfer. The N 1s of MXene/Zn-HMT50, MCN50 (Figure 2f) could be fitted with three component peaks located at binding energies of 398.8, 400.1, and 401.8 eV, respectively, corresponding to pyridinic-N (N-6), pyrrolic-N (N-5) and graphitic-N (N-Q) bonds.[17] The relative atomic proportions in the N 1s of MCN50

ADVANCED
SCIENCE NEWS

www.advancedsciencenews.com

NANO · MICRO

small

www.small-journal.com

are listed in Table S3. Graphitic-N has the capability to increase the electrode conductivity, while pyridinic-N and pyrrolic-N can efficiently endow the electrode with more active sites, thereby introducing additional pseudocapacitance.[29]

## 2.2. Electrochemical Performance of MCN Electrodes

### 2.2.1. Three-Electrode Configuration

**Figure 3** presents the electrochemical performance of MCNs in the three-electrode configuration. Figure 3a shows CV curves of MXene, MCN40, MCN50, and MCN60 between −0.9 and −0.1 V at 20 mV s$^{-1}$. All MXene and MCN electrodes demonstrate CV profiles with oxidation and reduction peaks, suggesting capacitance contribution from the Faraday redox reaction, and the reactions are as follows in Equation (1):[30]

$$Ti_3C_2O_x(OH)_yF_z + \delta e^- + \delta H^+ \leftrightarrow Ti_3C_2O_{x-\delta}(OH)_{y+\delta}F_z \qquad (1)$$
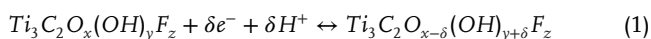
It should be noted that the enclosed CV areas of MCN electrodes are significantly greater than that of MXene, indicating a larger capacitance. Figure 3b shows GCD curves of these electrodes at 2 A g$^{-1}$. The GCD curves display approximately symmetrical nonlinear profiles that deviate from the triangular shape characteristic of the electric double-layer capacitor, further confirming the pseudocapacitive energy storage mechanism.[31] Moreover, MCN50 has the longest discharge time, suggesting an optimum capacitive performance, which agrees well with the CV results. The introduced nitrogen increases the electronegativity of MCN electrodes. The graphitic-N promotes the adsorption/separation of hydrogen ions in the electrolyte to form double-layer capacitance, while pyrrolic-N and pyridinic-N carries out oxidation-reduction reaction, as illustrated in Equations (2) and (3):[32]

$$C_xN_y + \delta e^- + \delta H^+ \leftrightarrow C_xN_yH_\delta \qquad (2)$$

$$C_xN_yO_Z + \gamma e^- + \gamma H^+ \leftrightarrow C_xN_y(OH)_Z \qquad (3)$$
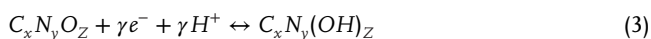
The CV curves of MCN50 at different scan rates are shown in Figure 3c. At lower scan rate, i.e., 5 mV s$^{-1}$, two pairs of wide and symmetrical redox peaks can be observed, where the cathode peaks are located at −0.83 V and −0.61 V, and the anode peaks are located at −0.77 V and −0.58 V, respectively. The symmetrical shape of GCD curves for MCN50 at different current densities (Figure 3d) indicates that the electrodes have superb capacitance reversibility and high Coulombic efficiency.[33] Furthermore, a negligible voltage drop is observed for MCN50, which may be attributed to the enhanced electrical conductivity by the introduction of pyridinic-N, pyrrolic-N, and graphitic-N.[34] The mass specific capacitance at different current densities (Figure 3e) suggests that the specific capacitance values for MXene, MCN40, MCN50, and MCN60 are 202.8 F g$^{-1}$, 371.9 F g$^{-1}$, 418.4 F g$^{-1}$, and 357.9 F g$^{-1}$, respectively. By comparing the work with other MXene composites, MCN50 has superior capacitive property (Table S4). In addition, CN also presents a specific capacitance of 115.9 F g$^{-1}$ at the same current density (Figure S10). The mass specific capacitance of MCN50 is 2.06

times that of pure MXene, 3.61 times that of CN. By increasing the proportion of Zn-HMT, the rate performance of MCN can be significantly improved (the capacitance retention rate of MXene, MCN40, MCN50, and MCN60 at the current density of 50 A g$^{-1}$ are 71.27%, 95.07%, 95.60%, 95.90%).

To better understand the ion and electron transfer, EIS is conducted on different electrodes. Figure 3f shows the Nyquist plots with a frequency range from 100 kHz to 10 mHz. The curves for various electrodes exhibit nearly vertical lines in the low-frequency region, suggesting nearly ideal capacitive characteristics. The diameter of semicircle in the high-frequency region indicates the interfacial charge transfer resistance ($R_{ct}$).[35] MCN40 (0.193 Ω), MCN50 (0.097 Ω), and MCN40 (0.083 Ω) have lower $R_{ct}$ than MXene (0.782 Ω), indicating that the intercalation of carbon nanosheets supports ion transfer. In addition, the transformed graphitic-N also facilitates the charge transfer process, favoring excellent power density and energy storage.[16,36] Although MCN60 exhibits the best electrical conductivity, the low content of MXene results in low capacitance. In order to achieve the trade-off between capacitance and conductivity, MCN50 is chosen for the following study.

To investigate the charge storage mechanism of MCN, CV data of MXene and MCN50 electrodes at various scan rates condition are analyzed. The relationship between the current ($i$) and the scanning rate ($v$) is expressed by Equation (4):[31]

$$i = av^b \qquad (4)$$

where $a$ and $b$ represent adjustable parameters. The parameter $b$ can be obtained by linearly fitting of the log($v$)-log($i$) plot. When the capacitance is generated through a diffusion-controlled process of battery-type Faradaic intercalation, $b$ is 0.5; whereas if the capacitance is produced through a non-diffusion controlled process, namely double layer capacitance and pseudocapacitance, $b$ is 1.[3] Figure S11 shows log($v$)-log($i$) plots and the $b$ values calculated for MXene and MCN50. The $b$ values of the anodic and cathodic peaks for MCN50 are larger than 0.75, suggesting that the capacitance is mainly controlled by non-diffusion process, which is attributed to pseudocapacitance caused by nitrogen doping and the fast ions transport through the porous channels.[32c]

The different electrodes charge storage capacity can be quantitatively evaluated through analyzing their current responses. The relationship between the current ($i$) and the scanning rate ($v$) relationship at a particular voltage ($V$) is as follows:

$$i(V) = k_1 v + k_2 v^{1/2} \qquad (5)$$

where $k_1 v$ and $k_2 v^{1/2}$ represent the capacitance contribution and diffusion-controlled contribution, respectively.[3,31] The capacitance-controlled parts of MCN50 and MXene measured at 50 mV s$^{-1}$ are highlighted in orange (Figure 3g; Figure S12a). The capacitance contribution ratios at the scan rates of 5, 10, 20, 50, and 100 mV s$^{-1}$ are 79.1, 81.7, 82.1, 87.7 and 94.8% for MCN50, and 63.0, 67.6, 73.1, 80.6, and 91.5% for MXene, respectively (Figure 3h; Figure S12b). The MCN50 has an excellent energy storage performance due to its high capacitive contribution from electrical double-layer capacitance and surface redox reactions.[37]

**ADVANCED
SCIENCE NEWS**

www.advancedsciencenews.com

NANO · MICRO

**small**

www.small-journal.com
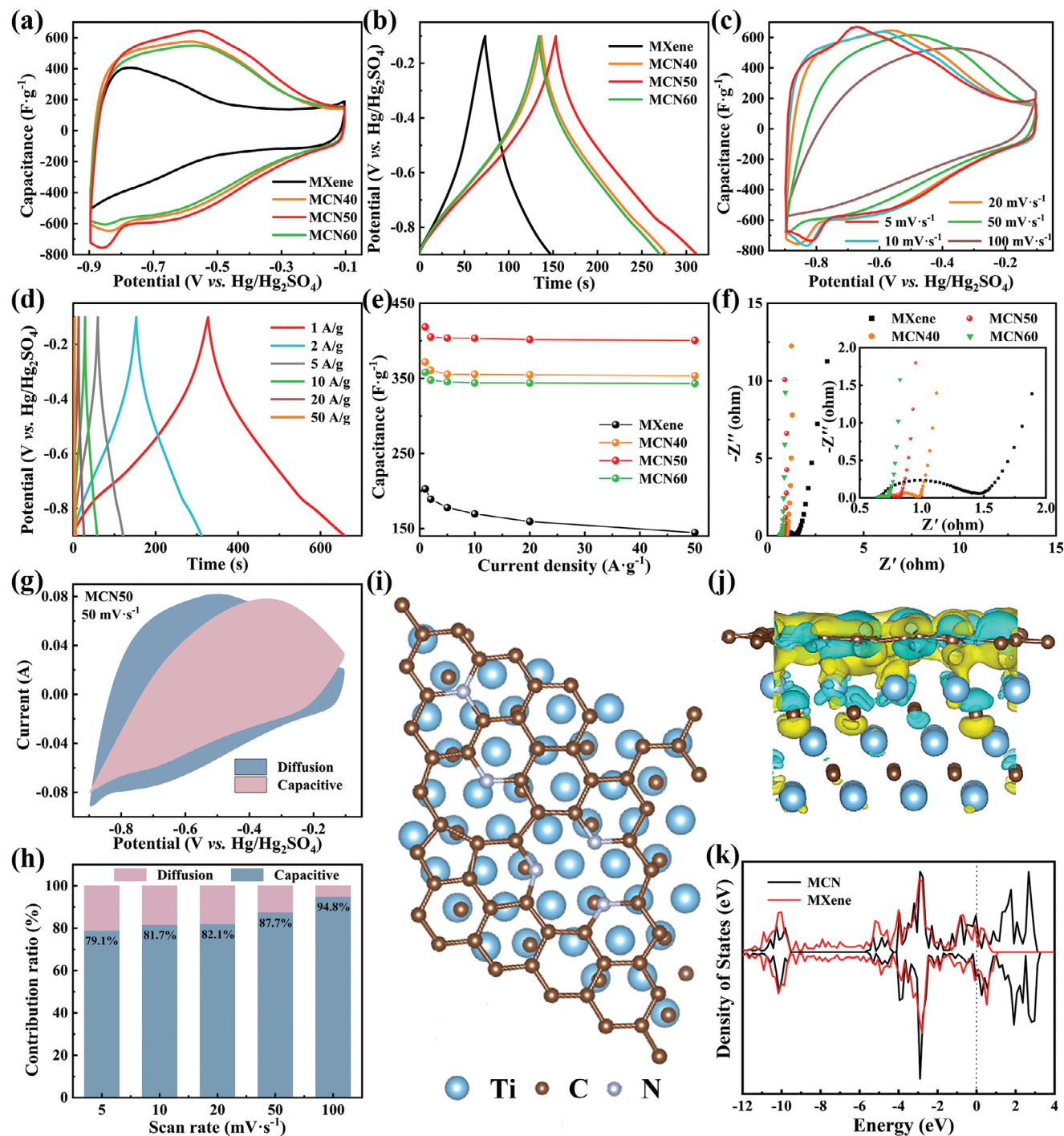
**Figure 3.** The electrochemical performance of MCNs in the three-electrode system. a) CV curves at a 20 mV s⁻¹ scan rate and b) various electrodes GCD curves at 2 A g⁻¹ current density. c) CV curves of MCN50 at different scan rates. d) GCD curves of MCN50 at different current densities. e) Rate performance of different electrodes. f) Nyquist plots of MXene, MCN40, MCN50, and MCN60. g) Capacitive contribution to the charge storage at 50 mV s⁻¹ and h) the percentage of capacitance contribution at different scan rates for MCN50. i) Top view and j) front view of MCN heterojunction structure. k) The densities of states (DOS) of MXene and MCN.

ADVANCED
SCIENCE NEWS

www.advancedsciencenews.com

NANO · MICRO
small
www.small-journal.com
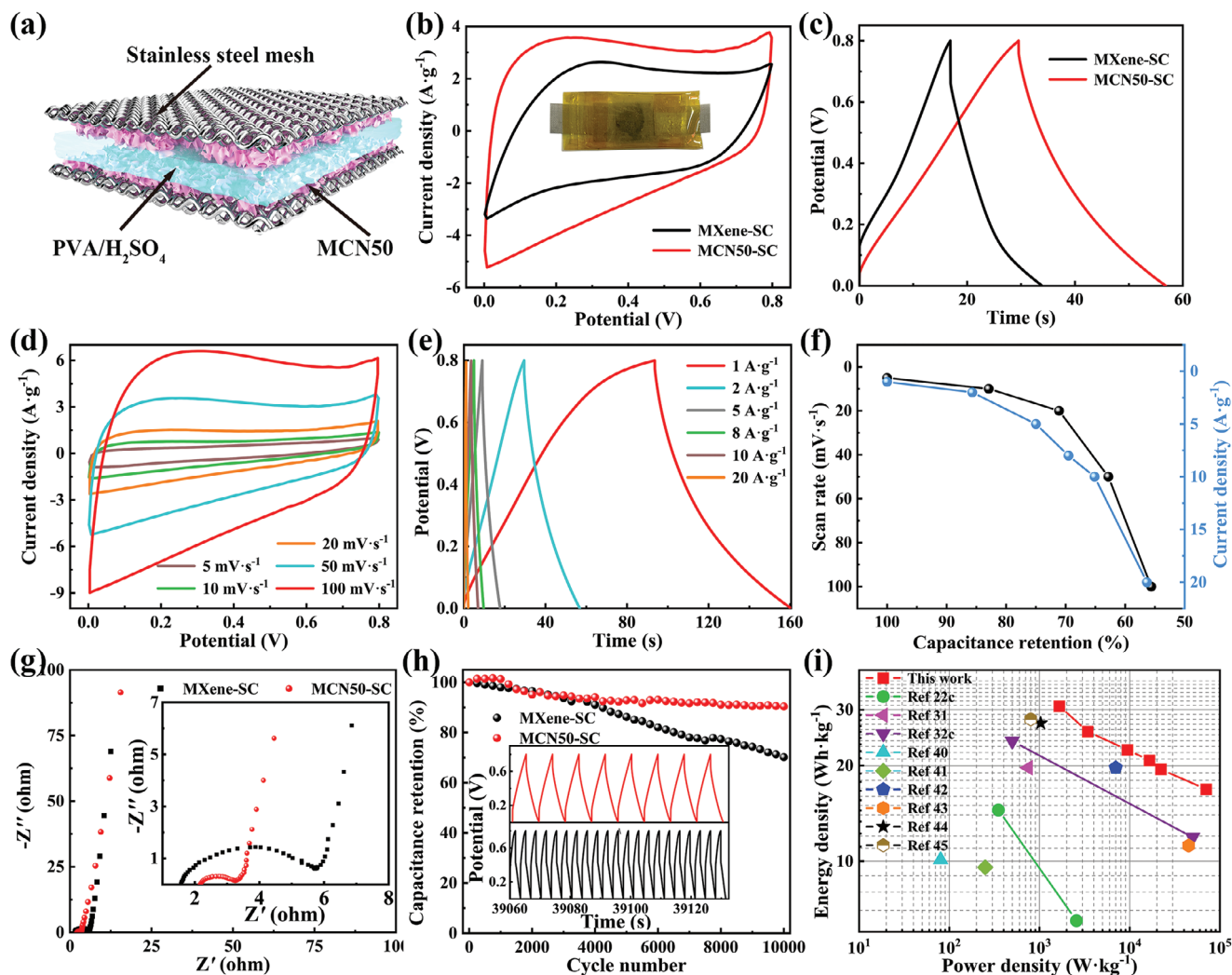
**Figure 4.** The electrochemical performance of MCN50-SC. a) The schematic representation of the all-solid supercapacitors. b) CV curves of MXene-SC and MCN50-SC at a scan rate of 10 mV s$^{-1}$ (the inset is the digital photograph of MCN50-SC). c) GCD curves of MXene-SC and MCN50-SC at a current density of 2 A g$^{-1}$. d) CV curves of MCN50-SC at different scan rates. e) GCD curves of MCN50-SC at different current densities. f) The rate performance of MCN50-SC at different scan rates and current densities. g) Nyquist plots of MXene-SC and MCN50-SC. h) The cycling stability of MXene-SC and MCN50-SC for 10 000 cycles at a current density of 10 A g$^{-1}$. i) Ragone plot of the energy density and power density of MCN50-SC device compared with other reports.

We then conduct the density functional theory (DFT) calculations using the Vienna Ab Initio Simulation Package (VASP) to assess the electrode's conductivity. The structure model of MCN is established (Figure 3i–j) based on XRD results, and the calculated lattice parameters closely resemble the experimental values. The projected density of states (PDOS) analysis suggests that the electrons of MCN can transit by overcoming smaller energy barriers near the Fermi level, indicating higher electrical conductivity than MXene (Figure 3k).

### 2.2.2. Symmetric All-Solid Supercapacitors

The electrochemical performance of a symmetric all-solid supercapacitor based on MCN50 (MCN50-SC) was investigated and shown in **Figure 4**. MCN50-SC is constructed by sandwiching

a thin piece gel electrolyte of PVA/H$_2$SO$_4$ between two MCN50 electrodes, as depicted in Figure 4a. The CV curves of MXene-SC and MCN50-SC at a scan rate of 50 mV s$^{-1}$ in the potential range of 0 to 0.8 V are shown in Figure 4b (the inset displays the digital photograph of MCN50-SC). The MCN50-SC exhibits larger CV integral areas than MXene-SC, which manifests that the former has better specific capacitance due to its expanded layer spacing and abundant nitrogen doping. MCN50-SC with higher specific capacitance also shows longer discharge time in GCD curves at a current density of 2 A g$^{-1}$ (Figure 4c). The CV curves of MCN50-SC in Figure 4d exhibit the characteristic rectangular shape without significant change when increasing the scan rate, suggesting an ideal capacitance performance.[38] In addition, the GCD curves of MCN50-SC in Figure 4e show an approximate isosceles triangle shape without distinct charge-discharge platforms under different current densities, indicating that the electrodes have
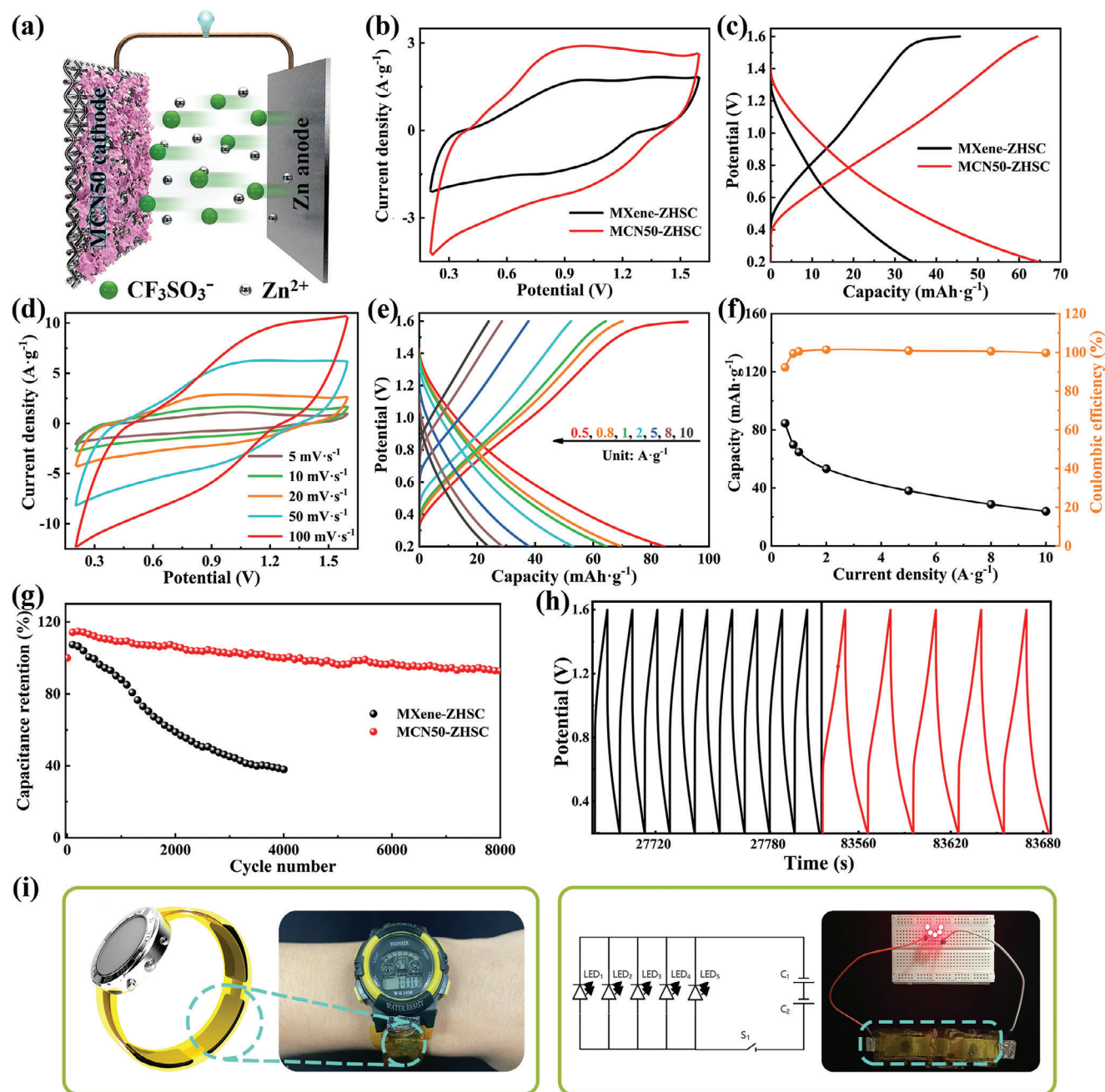
**Figure 5.** Application of MCN50 for ZHSC. a) Schematic illustration of ZHSC consisting of MCN50 cathode and Zn anode. b) CV curves of MXene-ZHSC and MCN50-ZHSC at a scan rate of 20 mV s$^{-1}$. c) GCD curves of MXene-ZHSC and MCN50-ZHSC at a current density of 1 A g$^{-1}$. d) The CV curves of the MCN50-ZHSC at various scan rates. e) GCD curves of the MCN50-ZHSC at different current densities. f) The rate performance and Coulombic efficiency of MCN50-ZHSC at different current densities. g,h) The cycling stability of MXene-ZHSC after 4000 cycles and MCN50-ZHSC after 8000 cycles at a current density of 5 A g$^{-1}$. i) Schematics and digital photo showing three MCN50-ZHSC connected in series powering up an electronic watch and five red light-emitting diodes.

exceedingly well reversibility during the charging and discharging process.[39] At a current density of 1 A g$^{-1}$, the mass specific capacitance reaches up to 336.4 F g$^{-1}$, and the corresponding power density and energy density are 1658.9 W kg$^{-1}$ and 30.8 Wh kg$^{-1}$, respectively. Furthermore, the MCN50-SC exhibits a power density of 70 541.4 W kg$^{-1}$ and still maintains an excellent energy

density of 16.9 Wh kg$^{-1}$ even at a high current density of 20 A g$^{-1}$.

The capacitance retention of MCN50-SC device is calculated from the CV and GCD curves under different scan rates and current densities (Figure 4f). It is found that the capacitance retention rates can be maintained at above 55%, even at a high scan rate of 100 mV s$^{-1}$ and a high current density of

ADVANCED
SCIENCE NEWS

www.advancedsciencenews.com

NANO · MICRO

small

www.small-journal.com

20 A g$^{-1}$, indicating a stable multiplicative performance and a low internal resistance of the MCN50-SC device. The Nyquist plots of MXene-SC and MCN-SC (Figure 4g) indicate that the interfacial charge transfer resistance ($R_{ct}$) of MCN50-SC (1.09 Ω) is smaller than that of MXene-SC (4.15 Ω), as the carbonization of Zn-HMT and nitrogen doping improves the conductivity. Moreover, the excellent cyclic stability of MCN50-SC is demonstrated with a capacitance retention of 90.4% after 10 000 cycles, which is about 20% higher than that of MXene-SC (Figure 4h). This MCN50-SC system offers superior energy and power density (Figure 4i) compared to the previously reported system, i.e., MXene/CNTs@Ni,[40] MXene/RGO/PEDOT:PSS,[31] CMFs//CCMP,[41] N-Ti$_3$C$_2$T$_x$,[32c] MXene/Graphdiyne nanotude,[22c] 3D-PMCF,[42] N-Co@CNR/rGO,[43] PPy-MXene-IL-mic,[44] N-doped goahne//MXene.[45]

### 2.2.3. Zinc-Ion Hybrid Supercapacitor

We next demonstrate the application of MCN50 electrode in zinc-ion hybrid supercapacitor (ZHSC, **Figure 5**) ZHSC was assembled by using the MCN50, Zn foil, and PVA/Zn(CF$_3$SO$_3$)$_2$ hydrogel as the cathode, anode, and electrolyte, respectively (Figure 5a). During the charging/discharging process, the rapid absorption/ desorption of electrolyte anion CF$_3$SO$_3^-$ on the surface of MCN50 materials is expected to achieve higher power density. Meanwhile, the reversible oxidation and reduction of Zn and Zn$^{2+}$ promise excellent energy density.[46] According to the CV and GCD results in Figure 5b,c, MCN50-ZHSC has a larger CV curve area and a longer discharge time, demonstrating its significantly higher specific capacity. In the Zinc-ion hybrid supercapacitor, the anode primarily undergoes a chemical redox reaction. During the charging process, Zn$^{2+}$ is reduced to Zn on the Zn foil, and during discharging, the Zn is oxidized to Zn$^{2+}$ in the electrolyte.[47] The CF$_3$SO$_3^-$ is absorbed on the MCN50 during charging, while the surface of MCN50 desorbs CF$_3$SO$_3^-$ and absorbs Zn$^{2+}$/H$^+$ during the discharging. The specific reactions are shown in the following equation:[46]

$$Zn^{2+} + 2e^- \leftrightarrow Zn \tag{6}$$

$$MCN50 + CF_3SO_3^- \leftrightarrow CF_3SO_3^- \parallel MCN50 \tag{7}$$
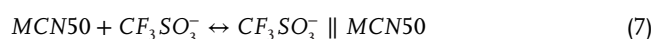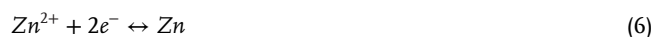
As the anodes in both MXene-ZHSC and MCN50-ZHSC are zinc foils, electrochemical performance of the devices is primarily influenced by the cathode.[29] Due to the intercalation of carbon nanosheets, MCN50 exhibits a significantly higher specific surface area compared to MXene, while the N incorporation can effectively improve the electrode electronegativity. These methods effectively enrich electrochemical active sites and enhances conductivity. The CV curves of MCN50-ZHSC in Figure 5d deviate significantly from the rectangular shape due to the asymmetric electrochemical behavior.[48]

Figure 5e presents the GCD curves for MCN50-ZHS acquired at various current densities with an indistinct plateau region, indicating that most capacity comes from the ion absorbed at structurally defective sites of MCN50. The capacity and Coulombic efficiency are also summarized (Figure 5f). The discharge capacity of MCN50-ZHSC device is 84.5 mAh g$^{-1}$ (251.3 F g$^{-1}$) at 0.5

A g$^{-1}$ current density, with a corresponding density of power of 403.5 W kg$^{-1}$ and an energy density of 68.4 Wh kg$^{-1}$. In comparison to other MXene-based supercapacitors, the MCN50-SC and MCN50-ZHSC in this study offer excellent energy and power density (Table S5). Besides, the Coulombic efficiency remains above 90% at diverse current densities. The MCN50-ZHSC also possesses excellent cycling performance in Figure 5g,h. After 8000 cycles at 5 A g$^{-1}$, the MCN50-ZHSC retains 93% of the initial capacitance, which is much higher than that of MXene-ZHSC (38% retention after 4000 cycles). In Figure 5i, we demonstrate to use MCN50-ZHSC units as a flexible wrist strap that can power a digital watch. Another demonstration involves using two MCN50-ZHSC units to power five red light-emitting diodes.

## 3. Conclusion

In summary, we describe a strategy for creating a structural composite electrode by intercalating MXene with highly nitrogen-doped carbon nanosheets (CN) to achieve a scaffold structure with larger specific surface area and more active sites. The electrical conductivity and capacitance are realized by a significant increase in graphitic-N and pyridinic-N. MCN50 (i.e., the mass ratio of Zn/HMT was 50%) exhibits the optimum electrochemical performance, delivering a specific capacitance of 418.4 F g$^{-1}$ at a current density of 1 A g$^{-1}$ in a three-electrode system, approximately 2.06 times that of pure MXene (202.8 F g$^{-1}$). The MCN50 electrode also demonstrates an excellent rate capability, with a capacitance retention rate of 95.6%. The all-solid-state symmetric supercapacitor with MCN50 delivers a high specific capacitance of 336.4 F g$^{-1}$ at a current density of 1 A g$^{-1}$, and reaches 30.8 Wh kg$^{-1}$ at a power density of 1658.9 W kg$^{-1}$. The assembled zinc ion hybrid supercapacitor exhibits high energy density of 68.4 Wh kg$^{-1}$, power density of 403.5 W kg$^{-1}$, and excellent cycling performance (i.e., the capacitance retention rate is 93% after 8000 cycles of charge-discharge). This approach opens a new window for the structural MXene electrode design for future high performance supercapacitor.

## Supporting Information

Supporting Information is available from the Wiley Online Library or from the author.

## Conflict of Interest

The authors declare no conflict of interest.

## Data Availability Statement

The data that support the findings of this study are available in the supplementary material of this article.

ADVANCED
SCIENCE NEWS

www.advancedsciencenews.com

NANO · MICRO
small
www.small-journal.com

## Keywords

[1] H. Zhang, L. Wang, X. Xing, S. Zhao, K. Wang, S. Liu, *Adv. Funct. Mater.* **2022**, *32*, 2208403.

[2] a) X. Wang, H. Li, H. Li, S. Lin, W. Ding, X. Zhu, Z. Sheng, H. Wang, X. Zhu, Y. Sun, *Adv. Funct. Mater.* **2020**, *30*, 0190302; b) L. Qin, G. Yang, D. Li, K. Ou, H. Zheng, Q. Fu, Y. Sun, *Chem. Eng. J.* **2022**, *430*, 133045.

[3] Y. Wang, X. Wang, X. Li, X. Li, Y. Liu, Y. Bai, H. Xiao, G. Yuan, *Adv. Funct. Mater.* **2020**, *31*, 2008185.

[4] G. Li, L. Wang, X. Lei, Z. Peng, T. Wan, S. Maganti, M. Huang, V. Murugadoss, I. Seok, Q. Jiang, D. Cui, A. Alhadhrami, M. M. Ibrahim, H. Wei, *Adv. Compos. Hybrid Ma.* **2022**, *5*, 853.

[5] Y. Wei, M. Zheng, W. Luo, B. Dai, J. Ren, M. Ma, T. Li, Y. Ma, *J. Energy Storage* **2022**, *45*, 103715.

[6] a) Y. Mu, L. Wang, R. Zhang, R. A. Pashameah, E. Alzahrani, Z. Li, A. K. Alanazi, H. Algadi, M. Huang, Z. Guo, T. Wan, H. Wei, *Appl. Surf. Sci.* **2023**, *613*, 155982; b) Z. Cai, Y.-F. Ma, M. Wang, A. N. Qian, Z.-M. Tong, L.-T. Xiao, S.-T. Jia, X.-Y. Chen, *Rare Met.* **2022**, *41*, 2084.

[7] M. S. Javed, X. Zhang, S. Ali, A. Mateen, M. Idrees, M. Sajjad, S. Batool, A. Ahmad, M. Imran, T. Najam, W. Han, *Nano Energy* **2022**, *101*, 107624.

[8] a) F. Zhu, W. Liu, Y. Liu, W. Shi, *Chem. Eng. J.* **2020**, *383*, 123150; b) J.-Q. Qi, M.-Y. Huang, C.-Y. Ruan, D.-D. Zhu, L. Zhu, F.-X. Wei, Y.-W. Sui, Q.-K. Meng, *Rare Met.* **2022**, *41*, 4116.

[9] a) D. Wen, G. Ying, L. Liu, Y. Li, C. Sun, C. Hu, Y. Zhao, Z. Ji, J. Zhang, X. Wang, *J. Alloy. Compd.* **2022**, *900*, 163436; b) Y. Wang, Y. Wang, *SmartMat* **2023**, *4*, e1130; c) Z.-L. Tan, J.-X. Wei, Y. Liu, F. Zaman, W. Rehman, L.-R. Hou, C.-Z. Yuan, *Rare Met.* **2022**, *41*, 775.

[10] a) D. Kong, Z. M. El-Bahy, H. Algadi, T. Li, S. M. El-Bahy, M. A. Nassan, J. Li, A. A. Faheim, A. Li, C. Xu, M. Huang, D. Cui, H. Wei, *Adv. Compos. Hybrid Ma.* **2022**, *5*, 1976. b) A. Chen, C. Wang, O. A. Abu Ali, S. F. Mahmoud, Y. Shi, Y. Ji, H. Algadi, S. M. El-Bahy, M. Huang, Z. Guo, D. Cui, H. Wei, *Compos. Part A: Appl. S.* **2022**, *163*, 107174; c) J.-Q. Qi, C.-C. Zhang, H. Liu, L. Zhu, Y.-W. Sui, X.-J. Feng, W.-Q. Wei, H. Zhang, P. Cao, *Rare Met.* **2022**, *41*, 2633.

[11] M. Dadashi Firouzjaei, S. K. Nemani, M. Sadrzadeh, E. K. Wujcik, M. Elliott, B. Anasori, *Adv. Mater.* **2023**, *35*, 2300422.

[12] a) X. Tang, J. Luo, Z. Hu, S. Lu, X. Liu, S. Li, X. Zhao, Z. Zhang, Q. Lan, P. Ma, Z. Wang, T. Liu, *Nano Res.* **2023**, *16*, 1755; b) Y. Wang, Y. Liu, C. Wang, H. Liu, J. Zhang, J. Lin, J. Fan, T. Ding, J. E. Ryu, Z. Guo, *Engineered Science* **2020**, *9*, 50.

[13] X. Gao, X. Du, T. S. Mathis, M. Zhang, X. Wang, J. Shui, Y. Gogotsi, M. Xu, *Nat. Commun.* **2020**, *11*, 6160.

[14] X. Wang, Y. Wang, D. Liu, X. Li, H. Xiao, Y. Ma, M. Xu, G. Yuan, G. Chen, *ACS Appl. Mater. Inter* **2021**, *13*, 30633.

[15] X. Ning, H. Huang, Y. Zhang, Z. Chen, Y. Guo, C. Li, Z. Fan, H. Tong, L. Pan, *Electrochim. Acta* **2022**, *435*, 141369.

[16] C. Lu, L. Yang, B. Yan, L. Sun, P. Zhang, W. Zhang, Z. Sun, *Adv. Funct. Mater.* **2020**, *30*, 2000852.

[17] a) S. Liu, J. Zhou, H. Song, *Adv. Energy Mater.* **2018**, *8*, 1800569; b) V. S. Sivasankarapillai, T. S. K. Sharma, K.-Y. Hwa, S. M. Wabaidur, S. Angaiah, R. Dhanusuraman, *ES Energy & Environment* **2022**, *15*, 4.

[18] J. Zheng, X. Pan, X. Huang, D. Xiong, Y. Shang, X. Li, N. Wang, W.-M. Lau, H. Y. Yang, *Chem. Eng. J.* **2020**, *396*, 125197.

[19] a) L. Ding, Y. Wei, L. Li, T. Zhang, H. Wang, J. Xue, L. X. Ding, S. Wang, J. Caro, Y. Gogotsi, *Nat. Commun.* **2018**, *9*, 155; b) S. u. Rehman, R. Ahmed, K. Ma, S. Xu, T. Tao, M. A. Aslam, M. Amir, J. Wang, *Engineered Science* **2020**, *13*, 71.

[20] Y. Zhu, J. Ciston, B. Zheng, X. Miao, C. Czarnik, Y. Pan, R. Sougrat, Z. Lai, C. E. Hsiung, K. Yao, I. Pinnau, M. Pan, Y. Han, *Nat. Mater.* **2017**, *16*, 532.

[21] a) R. Guo, X. Liu, B. Wen, F. Liu, J. Meng, P. Wu, J. Wu, Q. Li, L. Mai, *Nano-Micro Lett.* **2020**, *12*, 148; b) F. Wang, C. Wang, G. Li, Y. Wang, W. Zhang, G. Shi, X. Yan, J. Shi, *Mater. Today Nano* **2023**, *23*, 100352; c) D. Deng, S. Wu, H. Li, H. Li, L. Xu, *Small* **2023**, *19*, 2205469.

[22] a) T. Bai, W. Wang, W. Gue, S. Li, W. Guo, M. Ye, C. Wu, *ACS Appl. Mater. Interfaces* **2021**, *13*, 57576; b) Z. Fan, J. Wang, H. Kang, Y. Wang, Z. Xie, Z. Cheng, Y. Liu, *ACS Appl. Energy Mater.* **2020**, *3*, 1811; c) Y. Wang, N. Chen, Y. Liu, X. Zhou, B. Pu, Y. Qing, M. Zhang, X. Jiang, J. Huang, Q. Tang, B. Zhou, W. Yang, *Chem. Eng. J.* **2022**, *450*, 138398.

[23] a) M. Dvoyashkin, D. Leistenschneider, J. D. Evans, M. Sander, L. Borchardt, *Adv. Energy Mater.* **2021**, *11*, 2100700; b) A. Udayakumar, P. Dhandapani, S. Ramasamy, S. Angaiah, *ES Energy & Environment* **2023**, *20*, 902.

[24] Z. Ling, C. E. Ren, M. Q. Zhao, J. Yang, J. M. Giammarco, J. Qiu, M. W. Barsoum, Y. Gogotsi, *Proc. Natl. Acad. Sci* **2014**, *111*, 16676.

[25] W. Tian, A. VahidMohammadi, M. S. Reid, Z. Wang, L. Ouyang, J. Erlandsson, T. Pettersson, L. Wagberg, M. Beidaghi, M. M. Hamedi, *Adv. Mater.* **2019**, *31*, 1902977.

[26] J. Zhang, N. Kong, S. Uzun, A. Levitt, S. Seyedin, P. A. Lynch, S. Qin, M. Han, W. Yang, J. Liu, X. Wang, Y. Gogotsi, J. M. Razal, *Adv. Mater.* **2020**, *32*, 2001093.

[27] M. Kota, X. Yu, S.-H. Yeon, H.-W. Cheong, H. S. Park, *J. Power Sources* **2016**, *303*, 372.

[28] M. Yao, Y. Chen, Z. Wang, C. Shao, J. Dong, Q. Zhang, L. Zhang, X. Zhao, *Chem. Eng. J.* **2020**, *395*, 124057.

[29] a) R. Zhao, H. Di, X. Hui, D. Zhao, R. Wang, C. Wang, L. Yin, *Energ. Environ. Sci.* **2020**, *13*, 246; b) F. Lai, C. Yang, R. Lian, K. Chu, J. Qin, W. Zong, D. Rao, J. Hofkens, X. Lu, T. Liu, *Adv. Mater.* **2020**, *32*, 2002474; c) W. Zong, N. Chui, Z. Tian, Y. Li, C. Yang, D. Rao, W. Wang, J. Huang, J. Wang, F. Lai, T. Liu, *Adv. Sci.* **2021**, *8*, 2004142; d) G. Zhang, G. Li, T. Heil, S. Zafeiratos, F. Lai, A. Savateev, M. Antonietti, X. Wang, *Angew. Chem., Int. Ed.* **2019**, *58*, 3433; e) F. Lai, Y.-E. Miao, L. Zuo, H. Lu, Y. Huang, T. Liu, *Small* **2016**, *12*, 3235.

[30] X. Huang, J. Huang, D. Yang, P. Wu, *Adv. Sci. (Weinh)* **2021**, *8*, 2101664.

[31] T. Zhao, D. Yang, S.-M. Hao, T. Xu, M. Zhang, W. Zhou, Z.-Z. Yu, *J. Mater. Chem. A* **2023**, *11*, 1742.

[32] a) H. M. Jeong, J. W. Lee, W. H. Shin, Y. J. Choi, H. J. Shin, J. K. Kang, J. W. Choi, *Nano Lett.* **2011**, *11*, 2472; b) Y. Wen, T. E. Rufford, X. Chen, N. Li, M. Lyu, L. Dai, L. Wang, *Nano Energy* **2017**, *38*, 368; c) M. Cai, X. Wei, H. Huang, F. Yuan, C. Li, S. Xu, X. Liang, W. Zhou, J. Guo, *Chem. Eng. J.* **2023**, *458*, 141338.

[33] Y. Wang, Y. Cui, D. Kong, X. Wang, B. Li, T. Cai, X. Li, J. Xu, Y. Li, Y. Yan, H. Hu, M. Wu, Q. Xue, Z. Yan, L. Zhao, W. Xing, *Carbon* **2021**, *180*, 118.

[34] Y. Yoon, M. Lee, S. K. Kim, G. Bae, W. Song, S. Myung, J. Lim, S. S. Lee, T. Zyung, K.-S. An, *Adv. Energy Mater.* **2018**, *8*, 1703173.

[35] M. Xia, J. Ning, X. Feng, H. Guo, D. Wang, J. Zhang, Y. Hao, *Chem. Eng. J.* **2022**, *428*, 131114.

[36] A. Amiri, Y. Chen, C. Bee Teng, M. Naraghi, *Energy Storage Mater.* **2020**, *25*, 731.

[37] F. Ran, T. Wang, S. Chen, Y. Liu, L. Shao, *Appl. Surf. Sci.* **2020**, *511*, 145627.

[38] J. Chen, H. Chen, M. Chen, W. Zhou, Q. Tian, C.-P. Wong, *Chem. Eng. J.* **2022**, *428*, 131380.

ADVANCED
SCIENCE NEWS

www.advancedsciencenews.com

NANO · MICRO
small
www.small-journal.com

[39] Y. Yu, A. Xu, Y. Zhang, W. Li, Y. Qin, *Chem. Eng. J.* **2022**, *445*, 136727.

[40] S. Li, Q. Zhang, L. Liu, J. Wang, L. Zhang, M. Shi, X. Chen, *J. Alloy. Compd.* **2023**, *941*, 168963.

[41] N. An, Z. Guo, C. Guo, M. Wei, D. Sun, Y. He, W. Li, L. Zhou, Z. Hu, X. Dong, *Chem. Eng. J.* **2023**, *458*, 141434.

[42] P. Zhang, Q. Zhu, R. A. Soomro, S. He, N. Sun, N. Qiao, B. Xu, *Adv. Funct. Mater.* **2020**, *30*, 2000922.

[43] H. Wu, D. He, Y. Wang, *Electrochim. Acta* **2020**, *343*, 136117.

[44] Q. Fan, R. Zhao, M. Yi, P. Qi, C. Chai, H. Ying, J. Hao, *Chem. Eng. J.* **2022**, *428*, 131107.

[45] D. Momodu, A. S. Zeraati, F. L. Pablos, U. Sundararaj, E. P. L. Roberts, *Electrochim. Acta* **2021**, *388*, 138664.

[46] Z. Li, D. Chen, Y. An, C. Chen, L. Wu, Z. Chen, Y. Sun, X. Zhang, *Energy Storage Mater.* **2020**, *28*, 307.

[47] a) Z. Fan, J. Jin, C. Li, J. Cai, C. Wei, Y. Shao, G. Zou, J. Sun, *ACS Nano* **2021**, *15*, 3098; b) T. Li, H. Wei, Y. Zhang, T. Wan, D. Cui, S. Zhao, T. Zhang, Y. Ji, H. Algadi, Z. Guo, L. Chu, B. Cheng, *Carbohydr. Polym.* **2023**, *309*, 120678.

[48] W. Zheng, J. Halim, Z. Sun, J. Rosen, M. W. Barsoum, *Energy Storage Mater.* **2021**, *38*, 438.